Article

Flexible Continuum Robot System for Minimally Invasive Endoluminal Gastrointestinal Endoscopy

Liping Sun [ID] and Xiong Chen *

School of Information Science and Technology, Fudan University, Shanghai 200438, China;
20110720094@fudan.edu.cn
* Correspondence: chenxiong@fudan.edu.cn

Abstract: This paper presents a minimally invasive surgical robot system for endoluminal gastrointestinal endoscopy through natural orifices. In minimally invasive gastrointestinal endoscopic surgery (MIGES), surgical instruments need to pass through narrow endoscopic channels to perform highly flexible tasks, imposing strict constraints on the size of the surgical robot while requiring it to possess a certain gripping force and flexibility. Therefore, we propose a novel minimally invasive robot system with advantages such as compact size and high precision. The system consists of an endoscope, two compact flexible continuum mechanical arms with diameters of 3.4 mm and 2.4 mm, respectively, and their driving systems, totaling nine degrees of freedom. The robot's driving system employs bidirectional ball-screw-driven motion of two ropes simultaneously, converting the choice of opening and closing of the instrument's end into linear motion, facilitating easier and more precise control of displacement when in position closed-loop control. By means of coordinated operation of the terminal surgical tools, tasks such as grasping and peeling can be accomplished. This paper provides a detailed analysis and introduction of the system. Experimental results validate the robot's ability to grasp objects of 3 N and test the system's accuracy and payload by completing basic operations, such as grasping and peeling, thereby preliminarily verifying the flexibility and coordination of the robot's operation in a master–slave configuration.

Keywords: surgical robot; minimally invasive endoluminal gastrointestinal endoscopy; flexible continuum mechanical arm

1. Introduction

Over the years, the incidence of gastrointestinal cancer has been steadily increasing [1]. Open surgery is the conventional approach for treating gastrointestinal cancer; however, it has significant drawbacks, including severe pain, high risk of bleeding, surgical site infections, and prolonged hospital stays. In contrast, minimally invasive surgery (MIS) is extensively researched due to its advantages, such as reduced pain, minimal trauma, and faster recovery, making it a potential method for treating gastrointestinal cancer [2,3]. In MIS, due to the limited surgical workspace, surgical instruments must navigate through narrow and curved channels. Therefore, small size and adequate flexibility are two important considerations in designing MIS instruments. To overcome the limitations of traditional MIS instruments and enhance surgeons' skills, minimally invasive surgical robots have become an important approach applied in clinical practice.

Minimally invasive surgery (MIS) can be categorized into single-port laparoscopy (SPL), multi-port laparoscopy, and natural orifice transluminal endoscopic surgery (NOTES). Recently, more researchers have shifted their focus from multi-port laparoscopy toward SPL [4,5] and NOTES [6] to achieve more minimally invasive treatment approaches. SPL laparoscopic surgery requires a single skin incision ranging from 12 mm to 50 mm in diameter [7]. Conversely, robots used for NOTES have diameters ranging from 5 mm to 14 mm, allowing surgery to be performed by inserting through natural orifices without

incisions [8,9]. However, due to the limitations imposed by entry ports, current surgical robots still face challenges in executing typical surgical maneuvers with dexterity [10]. Moreover, within the confined spaces of the human natural orifices, robots struggle to avoid collisions with the human body, leading to potential injury [11]. In summary, size and flexibility are two critical factors in the ongoing improvement of MIS.

Furthermore, minimally invasive surgery (MIS) based on surgical robots can eliminate some limitations of traditional open surgery, and robot-assisted surgery has been proven to be a feasible solution [12,13]. The workspaces of NOTES and SPL surgeries are typically narrow and tortuous, surrounded by fragile blood vessels, nerves, and sensitive tissues. Therefore, the use of surgical robots equipped with flexible manipulators has become a crucial requirement for performing minimally invasive precision surgery [14,15]. To overcome the inherent limitations of MIS while addressing the inherent deficiencies of robotic information systems, the adoption of miniature robotic hands equipped with flexible mechanical arms has been introduced as a practical method. Advanced robotic technology has already been integrated into the practice of minimally invasive surgery [16].

Several research groups have developed a range of minimally invasive surgical robots. Jin et al. [17] designed a flexible surgical instrument for laparoscopic surgery, which features a flexible tube and end, eliminating the arm mechanism, thus reducing the volume of the surgical system, and avoiding the risk of interference between multiple instruments. Lara Harvey et al. [18] developed a novel endoscopic robot using concentric tube robots to address the challenge of applying endoscopic instruments in confined spaces, such as the bladder and uterus. Gao et al. [19], building upon previous research, developed the first robot simulator for the GESR system (GESRsim) to enhance surgeons' proficiency in operating surgical robots. Lau et al. [20] designed a dual-arm master–slave surgical robot for endoscopic submucosal dissection, featuring a customizable workspace. However, this dual-arm robot has fewer than three degrees of freedom, hence lacking flexibility. Researchers have made numerous attempts to enhance the flexibility of surgical robots. Innovations such as EndoMaster [21], STRAS [22], and PETH [23] have explored novel approaches to navigate through narrow and tortuous natural orifices. However, in clinical applications, they still suffer from drawbacks, such as large outer diameters, insufficient force feedback, and inaccurate operation [24–27].

In the design of surgical robots, various forms of mechanical arms are considered, including rigid articulated arms [28], rigid parallel arms [29], and flexible arms [30,31]. Among them, the rigid articulated arm is a serial structure known for its precise positioning and relatively good flexibility. However, when applied in minimally invasive gastrointestinal surgery, the multi-joint structure of serial articulated arms is complex. The robot relies on an endoscopic platform, and the digestive tract is constantly undergoing peristalsis, resulting in the robot lacking fixed support points, making it difficult to demonstrate precision. Additionally, the serial structure is relatively large in size, requiring more significant surgical space, which does not align with our design goal of reducing the robot's size. Rigid parallel robotic arms offer advantages such as high stability and smaller size. However, the range of motion of parallel robotic arms is limited, and they lack flexibility. Considering the above analysis and design objectives, we have chosen flexible continuum robotic arms as the arm structure for our designed robot. This choice is based on their strong adaptability and compact size. This study aims to address the current issues of large volume and insufficient flexibility in similar devices. A smaller device volume reduces patient trauma, alleviating postoperative discomfort. A comparison with other devices is shown in Table 1.

In this study, we have designed a minimally invasive surgical robot system to support minimally invasive gastrointestinal endoscopic surgery. This flexible robot is capable of better adapting to narrow and tortuous natural orifices, exhibiting excellent flexibility.

Table 1. Comparative study.

Device	Size	Flexibility (Degrees of Freedom, DOF)	Applications of Surgical Robots
Our Work	2.4 mm, 3.4 mm	9	Minimally invasive endoscopic gastrointestinal surgery
[17]	5~12 mm	4	Laparoscopic surgery
[18]	3 mm	8	Hysteroscopic surgery
[19]	3.5 mm, 2.5 mm	8	Endoscopic submucosal dissection
[20]	5 mm	2	Laparoscopic surgery
[16]	8 mm	3	Tonsillectomy
[14]	4 mm	6	Endoscopic mucosal resection (EMR)
[21]	10 mm	5	Robot-assisted endoscopic surgery
[13]	11 mm	5	Appendectomy and nephrectomy
[32]	4 mm	4	Maxillary sinus surgery

The main contributions of our research are summarized as follows:

- We have developed a minimally invasive surgical robot system with a compact mechanical structure. The diameter of the manipulator is only 3.4 mm, and the electrosurgical knife diameter is 2.4 mm. Utilizing a flexible mechanical arm, this robot exhibits outstanding flexibility with 9 degrees of freedom, while also possessing a sufficient gripping force (>3 N).
- The driving system employs a design where two ropes are simultaneously driven by bidirectional ball screws. This design converts the motion of opening and closing the forceps at the instrument's head into a linear motion, aiming to facilitate more precise control of displacement during closed-loop positioning control and improve system accuracy.
- We conducted a theoretical analysis of the robot, along with testing the robot's gripping force and flexibility. Finally, we performed in vivo experiments to validate the robot's performance in basic operations.

The remainder of this paper is organized as follows: Section 2 describes the whole robot system, including the manipulator, the electric knife, and their drive sections and control system block diagrams. Section 3 describes the theoretical foundation of robotics. Section 4 encompasses the experiments and analysis of the robot. Finally, the research findings are summarized in Section 5.

2. Materials and Methods

2.1. System Overview

As illustrated in Figure 1, the endoscopic surgical robot system consists of various modules, with the manipulator section comprising left and right manipulators. The right manipulator comprises a drive controller, Maxon servo motors, and a 6-degree-of-freedom flexible continuum robotic arm. The left manipulator includes a drive controller, Maxon servo motors, and a 3-degree-of-freedom high-frequency electric knife. The CCD imaging module consists of an endoscope, a CCD imaging sensor, and a set of cold light sources for the endoscope. The central control module comprises an industrial computer (GaLiL-DMC-4183, GaLiL, Rocklin, CA, USA) and a medical monitor. The industrial computer acquires images from the CCD imaging sensor attached to the endoscope and displays these images on the screen.
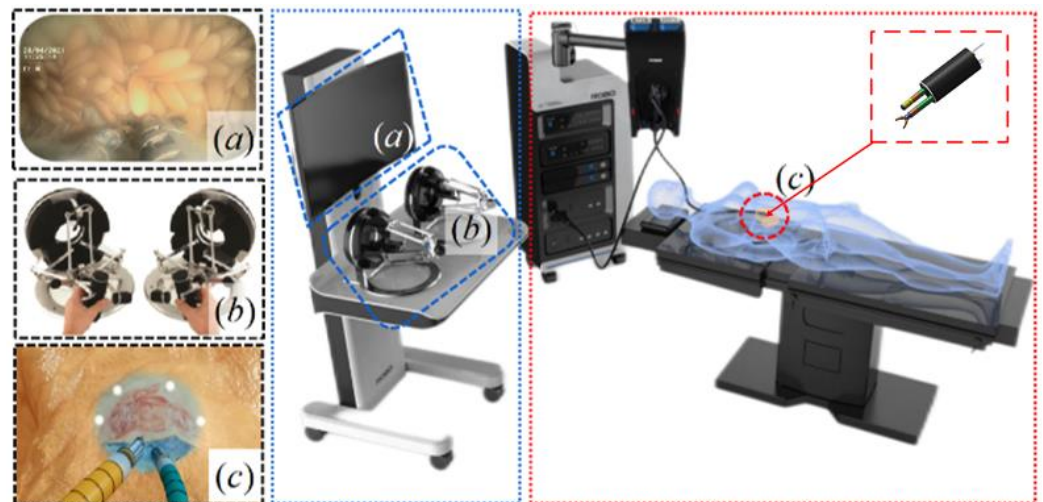
Figure 1. System diagram of the proposed endoscopic surgery robot. (**a**) Monitor of the CCD imaging module. (**b**) Master manipulator: Omega.7 provides configurations for the left and right manipulator configurations. (**c**) Slave manipulator: left and right slave manipulators, and the endoscope.

The left and right miniature flexible manipulators designed in this study are depicted in Figure 2, comprising flexible miniature robotic arms and flexible miniature electric knives (Figure 2a), detachable drive systems for left and right manipulators (Figure 2c,d), and a schematic diagram of the robotic system based on the endoscope platform. The smaller the volume of the endoscope platform, the lesser the impact on the patient. We selected an endoscope with a total diameter of 12 mm, featuring two instrument channels with maximum diameters of 3.7 mm and 2.8 mm, respectively. This necessitates the instruments to have smaller dimensions to pass through the endoscope platform (Figure 2b).
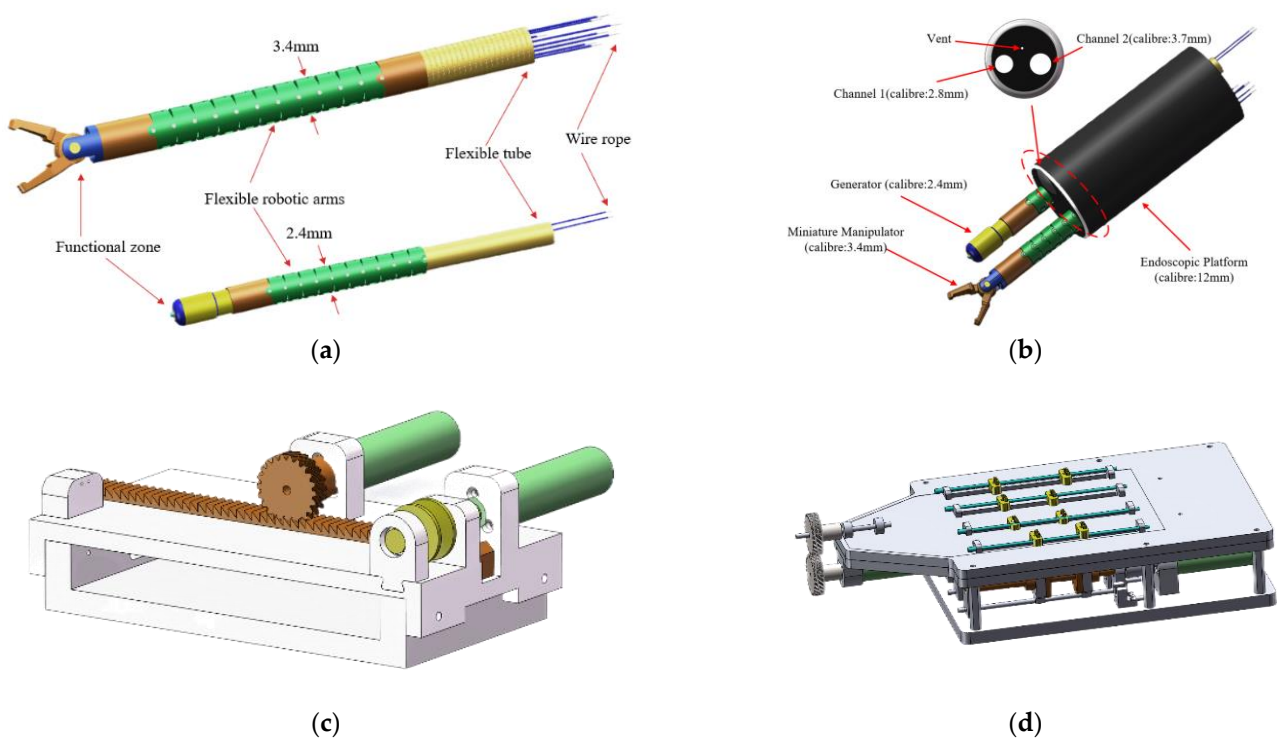

Figure 2. Flexible robotic system. (**a**) Robotic arm and electric knife. (**b**) Schematic diagram of endoscope platform. (**c**) Electric knife drive system. (**d**) Robotic arm drive system.

2.2. Manipulators

The manipulator is divided into left and right parts. The right manipulator consists of a clamp, a flexible continuum manipulator, and a steel wire rope with a hose. The diameter of the miniature mechanical hand is 3.4 mm, compact in structure, and made of 304 stainless steel. The material of the steel wire rope is also 304 stainless steel, and the hose of the steel wire rope is made of medical polytetrafluoroethylene hose. The left manipulator includes a high-frequency electric knife, a flexible continuum manipulator, and a steel wire rope with a hose, with a diameter of 2.8 mm. The electric knife was the KD-650L product from Olympus Corporation (Tokyo, Japan) and was modified. The flexible continuum manipulator arms of the two manipulators are composed of parts, as shown in Figure 3, made of 304 stainless steel, designed with a hollow structure (inner diameter: 2.6 mm) to facilitate the smooth passage of the steel wire rope with a hose (inner diameter: 0.2 mm), while the arc design structure ensures unhindered movement of the manipulator arms during operation, thereby possessing excellent motion performance. Spring tubes are used to transmit power from the drive to the functional area, using steel wire spring tubes (single-strand wire hollow tubes) from Asahi Intecc Corporation (Seto, Japan), to maintain sufficient flexibility to ensure that the robot's functional area can smoothly enter complex and tortuous human natural passages. Furthermore, the separation design of the drive and manipulator arms ensures the lightness and flexibility of the robot, making it more suitable for practical application needs.

(**a**)   (**b**)   (**c**)   (**d**)

Figure 3. Components of the flexible robotic arm. (**a**) Exploded view. (**b**) Front view. (**c**) Left view. (**d**) Top view.

The robotic arm has six degrees of freedom (DOFs), including DOFs for arm rotation, arm translation, two bending DOFs, and two DOFs for arm grippers. The electric knife has three DOFs, including DOFs for knife rotation and translation, and a bending DOF for the knife. Considering the necessity for maximum flexibility during the series of lateral incisions along the submucosal plane performed by the high-frequency electric knife (ESD) [33], the design of the electric knife's flexible robotic arm aims to provide additional flexibility for horizontal movements, as depicted in Figure 4.
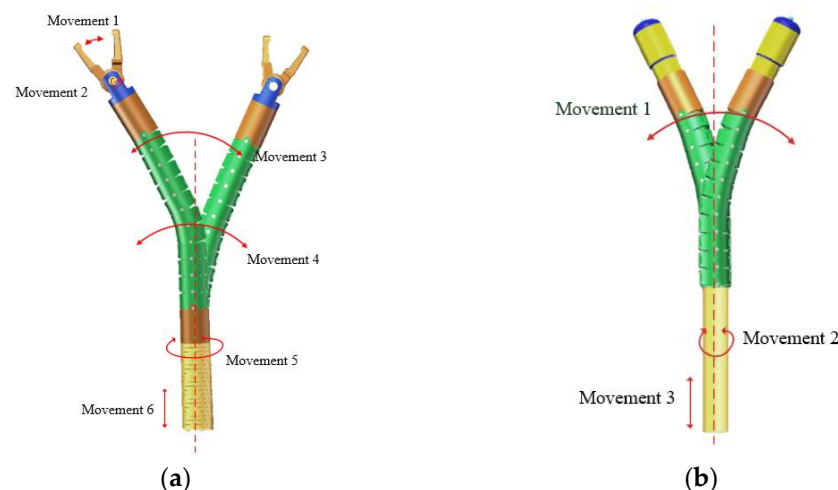

(**a**)   (**b**)

Figure 4. Robot's motion states. (**a**) Robotic arm. (**b**) Electrosurgical knife.

2.3. Drive Systems

Figure 5 presents a schematic diagram of the drive structure for the electric knife and the mechanical hand. These structures are designed to be detachable, which helps to facilitate timely replacement during surgery to meet different functional requirements. The drive system of the mechanical hand adopts a design where two-way ball screws simultaneously drive the movement of two ropes, converting the selective motion of the instrument head end into linear motion. This design aims to make it easier to precisely control the displacement when in position closed-loop control, thereby improving the system accuracy. The drive system of the electric knife adopts a structure design of gears and racks with a winding wheel, completing the motion of the electric knife by driving two ropes.
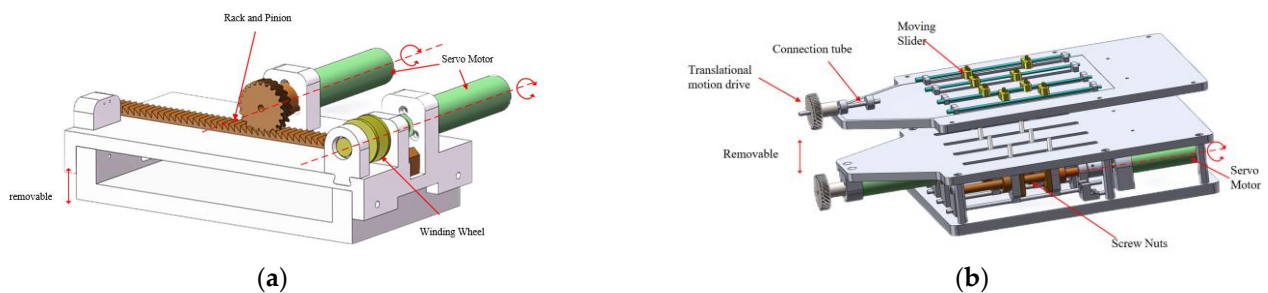

(**a**)

(**b**)

Figure 5. Drive system schematic. (**a**) Electrosurgical knife. (**b**) Robotic arm.

The wire ropes with hoses are connected to the sliders of the driver, while the sliders of the manipulator are connected to the support rod of the screw nut. The screw nut is driven by a servo motor (RE13, Maxon Motor Company), enabling the slider to move along the support rod. The connection between the robotic arm and the drive system is illustrated in Figure 6. The wire ropes with flexible tubes labeled as ① and ④ are connected to one clamp, while those labeled as ② and ③ are connected to another clamp. Through these wire ropes, the drive system can control the rotation and gripping movements of the robotic arm. The wire ropes with flexible tubes labeled as ⑥ and ⑦ are connected to the far-end flexible robotic arm to control its bending. The wire ropes with flexible tubes labeled as ⑤ and ⑧ are connected to the near-end flexible robotic arm to control its bending.
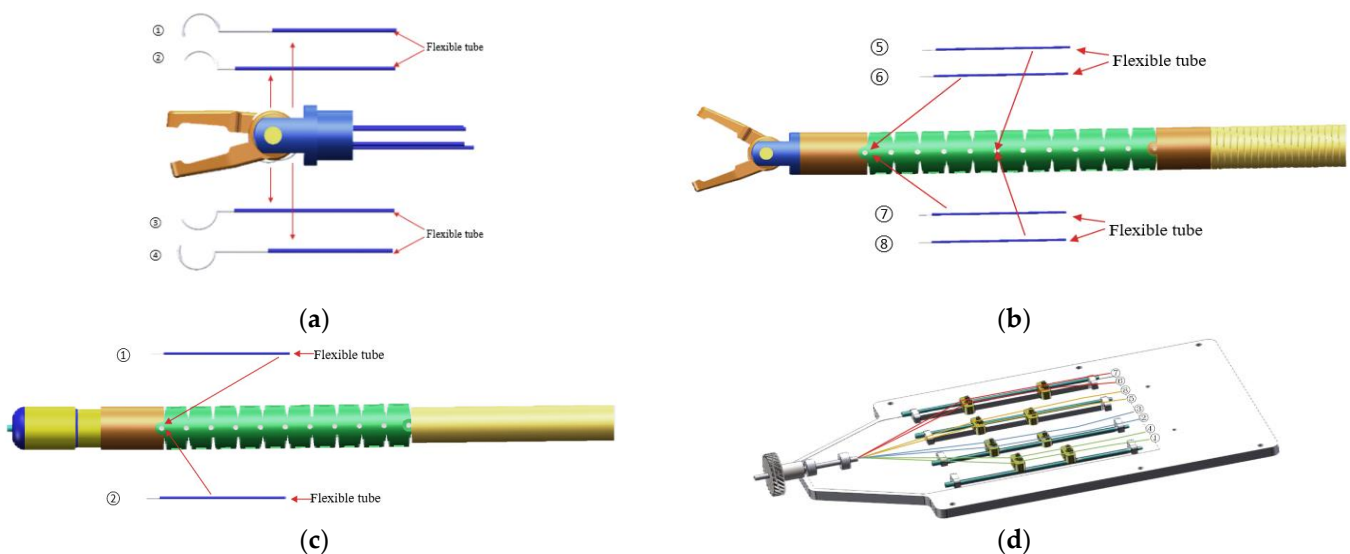

(**a**)

(**b**)

(**c**)

(**d**)

Figure 6. Connections of robot's wires. (**a**) Wires at the robotic arm gripper. (**b**) Wires at the robotic arm. (**c**) Electrosurgical knife wires' connection. (**d**) Wires of the robotic arm connected to the drive system.

2.4. Drive Systems

When operating the left and right master manipulators, the control software runs on the industrial computer, continuously acquiring real-time information about the master manipulators' position, orientation, angles, and grasping forces. Simultaneously, the control signals, calculated using the master–slave mapping formulas, are transmitted via the TCP/IP protocol to the drive controllers. The drive controllers utilize pulses to control the speed and position of the servo motors while synchronously receiving encoder signals from the servo motors to achieve a rapid response. In summary, the drive controllers independently control the movement of the left and right slave manipulators.

In the flexible arm surgical robot, the endoscope, the left slave manipulator, and the right slave manipulator enter the digestive tract transorally through a flexible tube. The endoscope can observe the position and orientation information of the end of the slave manipulators and the image information of the muscle tissue in real time. The system block diagram and signal flow diagram are shown in Figure 7.
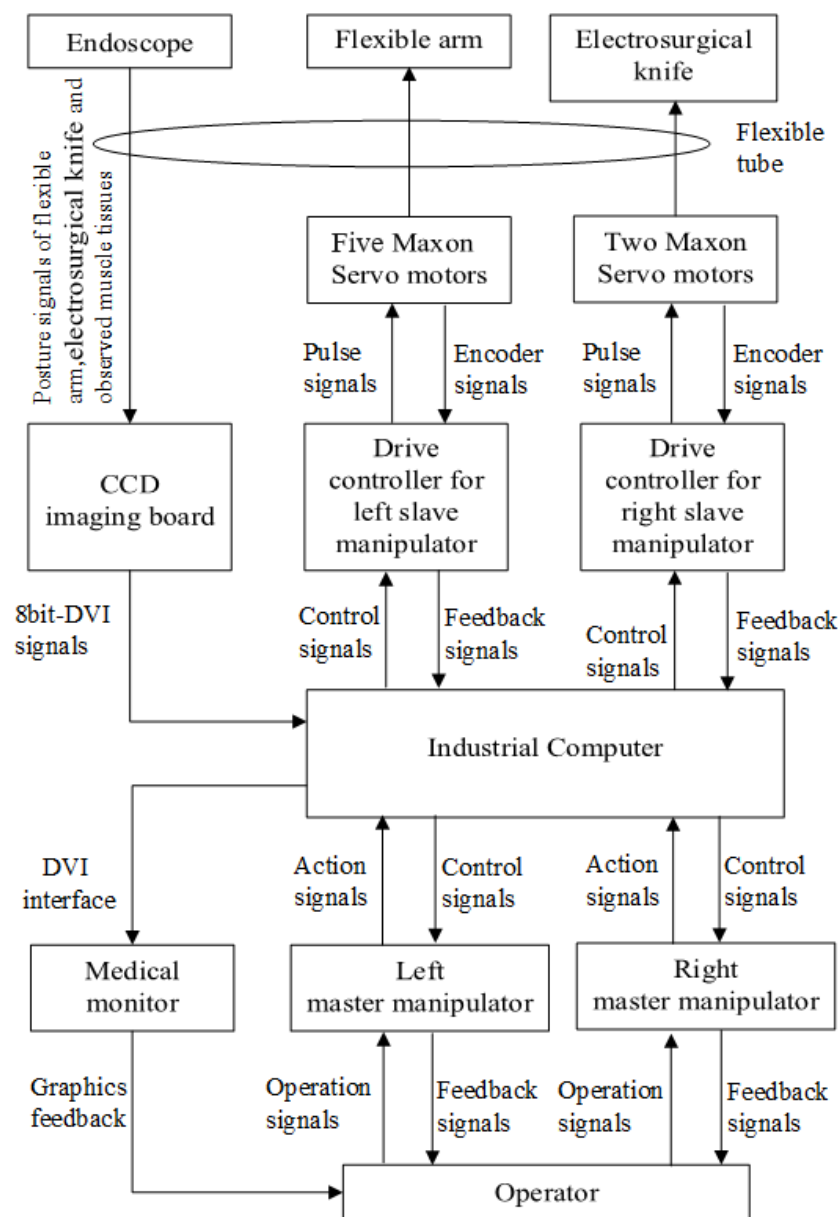

Figure 7. System block diagram and signal flow chart.

3. Theoretical Analysis

3.1. Kinematics

The kinematic analysis of robots holds significant importance for workspace analysis, motion trajectory planning, and feasibility assessment of robots. Hence, it is necessary to establish a kinematic model for analyzing the relevant kinematics [34]. There are currently many methods for kinematic modeling of flexible manipulator arms [35,36]. Considering that the flexible manipulator arm proposed in this paper is connected through mechanical structure engagement, with steel wires welded only at the proximal and distal ends, and has only two bending sections, a piecewise constant-curvature method was adopted to establish the kinematic model of the flexible continuum robot. A Cartesian coordinate system was established, where x, y, and z represent the coordinates of the end-effector of the continuous-body mechanical arm in the Cartesian coordinate system, while α and θ represent the rotation angle and bending angle of the mechanical arm, respectively. A geometric theoretical model of a single-segment continuous-body mechanical arm, as shown in Figure 8, was established. A coordinate system $\{O_i\}$ was established at the bottom center of the continuous-body mechanical arm, and a coordinate system $\{O_{i+1}\}$ was established at the top. The x-axis of the coordinate system points to one of the driving cables, the z-axis is along the axis direction, and the y-axis is determined by the right-hand rule. After multiple translations and rotations, the transformation matrix from the coordinate system $\{O_i\}$ to $\{O_{i+1}\}$ was obtained. Therefore, the homogeneous transformation matrix from $\{O_i\}$ to $\{O_{i+1}\}$ can be derived as:

$$_{i+1}^{i}T = rot(z, -\alpha_i)trans(0, 0, R_i \sin\theta_i)trans[R_i(1 - \cos\theta_i), 0, 0]rot(y, \theta_i)rot(z, \alpha_i) \quad (1)$$

where i represents the number of segments of the flexible continuous-body mechanical arm, and R_i is the bending radius of that segment of the mechanical arm.
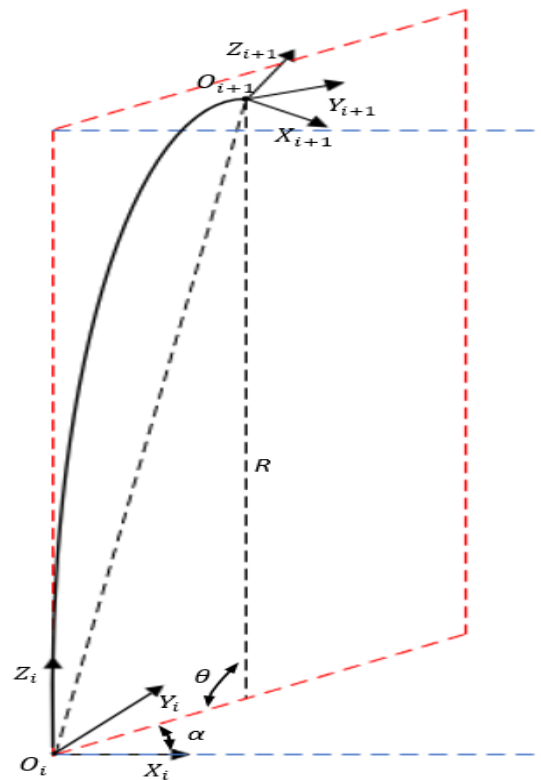

Figure 8. Geometric theoretical model of a single-segment continuous-body mechanical arm.

3.1.1. Electric Scalpel Kinematic Model

Based on the geometric theoretical model of a single-segment continuous-body mechanical arm, the kinematic model of the electric scalpel was established using the piecewise constant-curvature method, as illustrated in Figure 9. A base coordinate system $\{O_0\}$ was established at the center of the electric scalpel's bottom, a coordinate system $\{O_1\}$ was set up at the starting end of the flexible mechanical arm, $\{O_2\}$ was positioned at the end, and $\{O_3\}$ was established at the end of the electric scalpel. In the base coordinate system, the z-axis is aligned with the axis direction, the x-axis points to the right side of the mechanical arm and is perpendicular to the z-axis, and the y-axis is determined by the right-hand rule. The orientations of the other coordinate system axes are consistent with the description in the previous text.
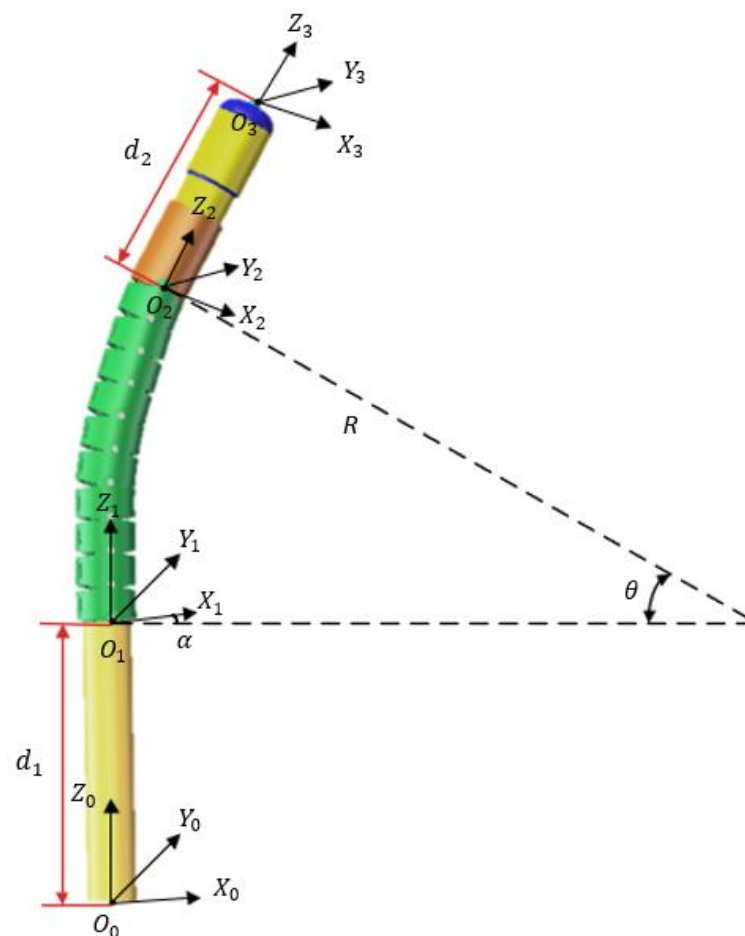

Figure 9. Kinematic model of the electric scalpel.

The end-effector position of the flexible continuous-body mechanical arm can be obtained by transforming from the configuration space using the homogeneous transformation matrices of both the global and local coordinate systems. Initially, by translating along the z-axis direction of the first translational segment by the axis length d_1, we obtained the homogeneous transformation matrix from the base coordinate system $\{O_0\}$ to coordinate system $\{O_1\}$:

$$
{}^{0}_{1}T = \begin{bmatrix} 1 & 0 & 0 & 0 \\ 0 & 1 & 0 & 0 \\ 0 & 0 & 1 & d_1 \\ 0 & 0 & 0 & 1 \end{bmatrix} \tag{2}
$$

By translating along the z-axis direction of the second translational segment by the axis length d_2, we obtained the homogeneous transformation matrix from coordinate system $\{O_2\}$ to coordinate system $\{O_3\}$:

$$\frac{2}{3}T = \begin{bmatrix} 1 & 0 & 0 & 0 \\ 0 & 1 & 0 & 0 \\ 0 & 0 & 1 & d_2 \\ 0 & 0 & 0 & 1 \end{bmatrix} \tag{3}$$

The homogeneous transformation matrix for the flexible continuous body was obtained through the multiplication of three homogeneous transformation matrices:

$$\frac{0}{3}T = \frac{0}{1}T\frac{1}{2}T\frac{2}{3}T = \begin{bmatrix} R & P \\ 0 & 1 \end{bmatrix} \tag{4}$$

where R is a 3×3 rotation matrix, and P is the end-effector position vector of the mechanical arm, expressed as:

$$P = [x_3\ y_3\ z_3]^T \tag{5}$$

$$\begin{cases} x_3 = d_2 c\alpha s\theta - \frac{Lc\alpha(c\theta-1)}{\theta} \\ y_3 = d_2 s\alpha s\theta - \frac{Ls\alpha(c\theta-1)}{\theta} \\ z_3 = d_1 + d_2 c\theta + \frac{Ls\theta}{\theta} \end{cases} \tag{6}$$

where s represents the sine function (sin), c represents the cosine function (cos), and L represents the length of the flexible continuous-body mechanical arm.

3.1.2. Kinematic Model of the Robotic Arm

The robotic arm model consists of two segments of flexible continuous-body mechanical arms and three known-length components. Using the piecewise constant-curvature method, the kinematic model was established, and its geometric model is depicted in Figure 10. The coordinate systems are defined as follows: a base coordinate system $\{O_0\}$ was established at the center of the robotic arm's base, a coordinate system $\{O_1\}$ was set up at the starting end of the proximal flexible mechanical arm, $\{O_2\}$ was positioned at the end of the proximal arm, $\{O_3\}$ was established at the starting end of the distal flexible mechanical arm, $\{O_4\}$ was established at the end of the distal arm, $\{O_5\}$ was established at the end of the second component, and $\{O_6\}$ was established at the end of the robotic arm. In the base coordinate system, the z-axis is aligned with the axis direction, the x-axis points to the left side of the robotic arm and is perpendicular to the z-axis, and the y-axis is determined by the right-hand rule. The orientations of the other coordinate system axes are consistent with the description in the previous text. Due to the mechanical structure constraints, the proximal and distal segments of the flexible mechanical arm were controlled for bending by two steel cables and cannot rotate independently. Hence, the rotation angles, α, for the proximal and distal segments of the mechanical arm were equal. Based on the single-segment kinematic model, a two-segment continuous-body mechanical arm was modeled using the piecewise constant-curvature method. The end-effector position of the flexible continuous-body mechanical arm can be obtained from the configuration space through the transformation matrices of both the global and local coordinate systems.

To obtain the homogeneous transformation matrix from the base coordinate system $\{O_0\}$ to coordinate system $\{O_1\}$, we started by translating along the z-axis direction of the first translational segment by the axis length d_1:

$$\frac{0}{1}T = \begin{bmatrix} 1 & 0 & 0 & 0 \\ 0 & 1 & 0 & 0 \\ 0 & 0 & 1 & d_1 \\ 0 & 0 & 0 & 1 \end{bmatrix} \tag{7}$$
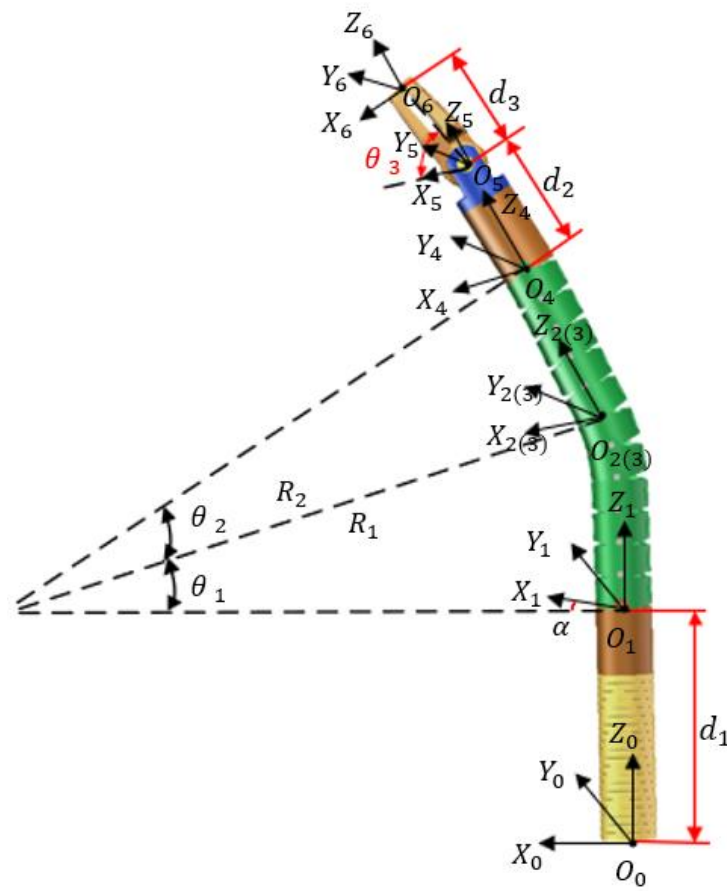
Figure 10. Kinematic model of the robotic arm.

Similarly, we obtained the homogeneous transformation matrix from coordinate system $\{O_2\}$ to coordinate system $\{O_3\}$:

$$
{}^2_3T = \begin{bmatrix} 1 & 0 & 0 & 0 \\ 0 & 1 & 0 & 0 \\ 0 & 0 & 1 & 0 \\ 0 & 0 & 0 & 1 \end{bmatrix}
\tag{8}
$$

The homogeneous transformation matrix for the proximal flexible continuous body was obtained through the multiplication of three homogeneous transformation matrices:

$$
{}^0_3T = {}^0_1T {}^1_2T {}^2_3T = \begin{bmatrix} R_1 & P_1 \\ 0 & 1 \end{bmatrix}
\tag{9}
$$

where R_1 is a 3×3 rotation matrix, and P_1 is the end-effector position vector of the proximal mechanical arm, expressed as:

$$
P_1 = \begin{bmatrix} x_3 \ y_3 \ z_3 \end{bmatrix}^T
\tag{10}
$$

$$
\begin{cases} x_3 = -\dfrac{L_1 c\alpha (c\theta_1 - 1)}{\theta_1} \\[2mm] y_3 = -\dfrac{L_1 s\alpha (c\theta_1 - 1)}{\theta_1} \\[2mm] z_3 = d_1 + \dfrac{L_1 s\theta_1}{\theta_1} \end{cases}
\tag{11}
$$

where s represents the sine function (sin), c represents the cosine function (cos), and L_1 represents the length of the proximal flexible continuous-body mechanical arm.

By translating along the z-axis direction of the second translational segment by the axis length d_2, we obtained the homogeneous transformation matrix from the base coordinate system $\{O_4\}$ to coordinate system $\{O_5\}$:

$$
{}^4_5T = \begin{bmatrix} 1 & 0 & 0 & 0 \\ 0 & 1 & 0 & 0 \\ 0 & 0 & 1 & d_2 \\ 0 & 0 & 0 & 1 \end{bmatrix} \tag{12}
$$

The homogeneous transformation matrix for the distal flexible continuous-body mechanical arm was obtained through the multiplication of five homogeneous transformation matrices:

$$
{}^0_5T = {}^0_1T {}^1_2T {}^2_3T {}^3_4T {}^4_5T = \begin{bmatrix} R_2 & P_2 \\ 0 & 1 \end{bmatrix} \tag{13}
$$

where R_2 is a 3×3 rotation matrix, and P_2 is the end-effector position vector of the distal mechanical arm, expressed as:

$$
P_2 = [x_5 \; y_5 \; z_5]^T \tag{14}
$$

$$
\begin{aligned}
x_5 = d_2 &[c\alpha c\theta_2 s\theta_1 - (sa)^2 s\theta_2 ca(1 - c\theta_1) + cas\theta_2(c\theta_1 c^2 a + s^2 a)] \\
&- \frac{[L_1 ca(c\theta_1 - 1)]}{\theta_1} + \frac{L_2 cas\theta_1 s\theta_2}{\theta_2} \\
&- \frac{[L_2 ca(c\theta_2 - 1)(c\theta_1 c^2 a + s^2 a)]}{\theta_2} \\
&+ \frac{[L_2(sa)^2 ca(1 - c\theta_1)(c\theta_2 - 1)]}{\theta_2}
\end{aligned} \tag{15}
$$

$$
\begin{aligned}
y_5 = d_2 &[sas\theta_2(c^2 a + c\theta_1 s^2 a) + sac\theta_2 s\theta_1 - (ca)^2 sas\theta_2(1 - c\theta_1)] \\
&- \frac{[L_1 sa(c\theta_1 - 1)]}{\theta_1} + \frac{L_2 sas\theta_1 s\theta_2}{\theta_2} \\
&- \frac{[L_2 sa(c\theta_2 - 1)(c\theta_1 s^2 a + c^2 a)]}{\theta_2} \\
&+ \frac{[L_2(ca)^2 sa(1 - c\theta_1)(c\theta_2 - 1)]}{\theta_2}
\end{aligned} \tag{16}
$$

$$
\begin{aligned}
z_5 = d_1 &- \frac{d_2[[(ca)^2 + (sa)^2]s\theta_1 s\theta_2 - c\theta_1 c\theta_2] + (L_1 s\theta_1)}{\theta_1} + \frac{(L_2 c\theta_1 s\theta_2)}{\theta_2} \\
&+ \frac{[[L_2 s\theta_1(c\theta_2 - 1)][(ca)^2 + (sa)^2]]}{\theta_2}
\end{aligned} \tag{17}
$$

where s represents the sine function (sin), c represents the cosine function (cos), and L_2 represents the length of the distal flexible continuous-body mechanical arm.

Furthermore, we obtained the end-effector coordinates of the robotic arm by further calculations:

$$
\begin{cases} x_6 = x_5 + d_3 s\theta_3 \\ y_6 = y_5 \\ z_6 = z_5 + d_3 c\theta_3 \end{cases} \tag{18}
$$

where s represents the sine function (sin) and c represents the cosine function (cos).

3.2. Establishment of Dynamic Models

3.2.1. Analysis of Dynamic Interaction Environment Model

The endoscopic system operates in a dynamically unknown environment during surgery. To analyze its motion characteristics and system response time, a model of the robot's operating environment system was established. By analyzing the characteristics of the interactive environment, a dynamic position-equivalent model approximating the

environment was created to account for the subjectivity in surgery. This was combined with the interaction model between the robot and the environment to establish a contact force model at the robot's end.

The uncertainty of the dynamic unknown environment model manifested in two aspects: (1) the stiffness of the environment is unknown or dynamic, and (2) the position of the environment changes dynamically. When the local characteristics of the unknown environment include uncertain environmental stiffness, let *F* be the contact established between the robot and the environment, representing the instantaneous contact force applied by the robot to the environment. Let *M* be the torque output by the motor. As shown in Figure 11, the end effector interaction model is known to have a dynamic environmental position *B*. The angle *β* is formed between the end of the manipulator *Xend* and the horizontal line of the dynamic environmental position. The angle *r* is formed between the end of the unknown environment and the horizontal line of the dynamic environmental position. The contact condition between the manipulator end and the dynamic unknown environment can be described by *β* and *r*.
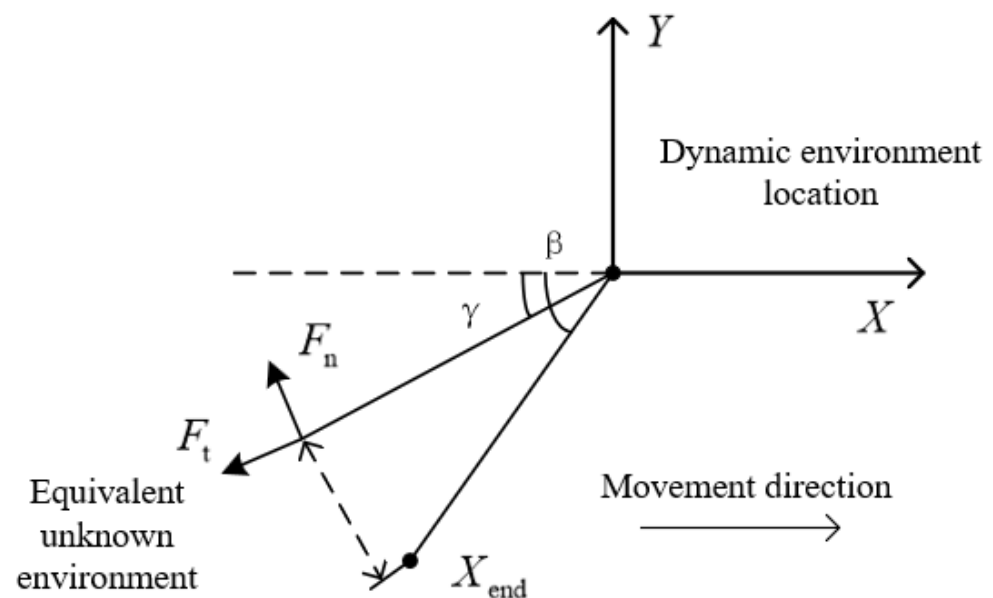

Figure 11. Robotic end interaction model.

When *β* = *r*, the contact is at a critical point; when *β* > *r*, the contact is in a deviated state; when *β* < *r*, contact force is generated. The instantaneous contact force *F* applied by the robot to the environment is known, as shown in Figure 11. *Fn* and *Ft* are the normal contact force and tangential contact force in the contact force model, respectively.

3.2.2. Kinematic Analysis of the Robotic Arm

The deformation of flexible bodies is highly complex, involving various coupled factors, making analytical expressions challenging. Hence, multiple discrete methods are commonly employed [37]. Simplification of the flexible arm and its end load involves neglecting rope mass and deformation [38], as depicted in Figure 12. Coordinate system X_0OY_0 represents the base coordinate system, while X_1OY_1 represents the joint coordinate system. X_0 denotes the direction of gravity, and X_1 points to the axis direction of the flexible arm before deformation. d_y represents the offset of the end load, perpendicular to X_1. The joint angle is denoted by *q*, the length of the flexible arm is *l*, and the cross-sectional height is h. The end load (robotic hand or electric scalpel) has a mass of m, *ρ* denotes the material density, *A* is the cross-sectional area, *E* represents the material's elastic modulus, and *I* stands for the moment of inertia of the cross-section.
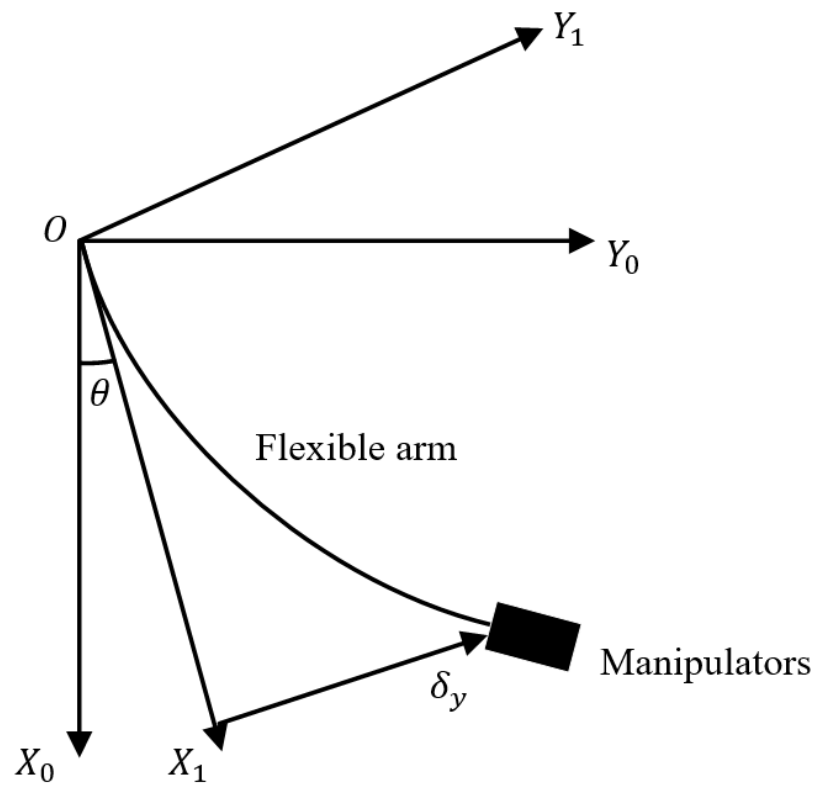
Figure 12. Simplified model of the flexible arm and end load.

To accurately establish the model of the flexible component and correctly describe its elastic deformation, modal analysis of the flexible arm-load system was conducted to determine its natural frequencies and corresponding mode shapes. Referring to [39], the differential equation governing the free vibration of a uniform material with a constant cross-section beam was obtained as follows:

$$\rho A \frac{\partial^2 d_y(x,t)}{\partial t^2} + EI \frac{\partial^4 d_y(x,t)}{\partial x^4} = 0 \tag{19}$$

Further referencing [40], the natural frequencies for each mode were obtained as follows:

$$\omega_i = \lambda_i^2 \sqrt{\frac{EI}{\rho A}} \tag{20}$$

where i = 1, 2, 3, ...

The mode shapes were obtained as follows:

$$\Phi_i(x) = \cos\lambda_i x - \cosh\lambda_i x + \frac{\cos\lambda_i l + \cosh\lambda_i l}{\sin\lambda_i l + \sinh\lambda_i l}(\sinh\lambda_i x - \sin\lambda_i x) \tag{21}$$

In practical applications, it is common to select the first n modes to achieve relatively high accuracy [40]. Considering that the robotic arm only has two degrees of freedom, a truncation frequency of the second order was chosen. Thus, the deformation of the flexible arm can be represented as [41,42]:

$$\delta_y(x,t) = q_1(t)\Phi_1(x) + q_2(t)\Phi_2(x) \tag{22}$$

By consulting [43], considering the length, *l* of the flexible arm of the robotic hand, the position vector of any point on the flexible arm in the base coordinate system is:

$$r(x,t) = \begin{bmatrix} cos\theta & -sin\theta & 0 \\ sin\theta & cos\theta & 0 \\ 0 & 0 & 1 \end{bmatrix} \begin{bmatrix} l \\ \delta_y(x,t) \\ 0 \end{bmatrix} \tag{23}$$

Without considering gravity, the kinetic energy of the robotic hand is:

$$E_{km} = \frac{1}{2}m\dot{r}(l,t)^T\dot{r}(l,t) \tag{24}$$

The kinetic energy of the flexible arm of the robotic hand is:

$$E_{kl} = \int_0^l \frac{1}{2}\rho A\dot{r}(x,t)^T\dot{r}(x,t)\mathrm{d}x \tag{25}$$

The elastic potential energy of the flexible arm of the robotic hand is:

$$E_{ul} = \int_0^l \frac{1}{2}EI\left(\frac{\partial^2 \delta_y(x,t)}{\partial x^2}\right)^2 \mathrm{d}x \tag{26}$$

According to Hamilton's principle, where T represents the system's kinetic energy, V represents the system's potential energy, and W represents the virtual work, it follows that:

$$\delta \int_{t_1}^{t_2} (T - V + W)\mathrm{d}t = 0 \tag{27}$$

The kinetic energy of the robotic hand's flexible arm itself is:

$$
\begin{aligned}
\delta \int_{t_1}^{t_2} E_{kl}\mathrm{d}t = \int_{t_1}^{t_2} &-\rho A[(2\gamma_3\dot{\theta}\dot{q}_2 q_2 + 2\gamma_6\dot{\theta}\dot{q}_1 q_2 + \gamma_1\ddot{\theta} + \gamma_2\ddot{\theta}q_1{}^2 + 2\gamma_6\ddot{\theta}q_1 q_2 \\
&+ 2\gamma_6\dot{\theta}\dot{q}_2 q_1 + \gamma_3\ddot{\theta}q_2{}^2 + \gamma_4\ddot{q}_1 + 2\gamma_1\dot{\theta}\dot{q}_1 q_1 + \gamma_5\ddot{q}_2)\delta\theta \\
&+ (-\gamma_2\dot{\theta}^2 q_1 + \gamma_2\ddot{q}_1 - \gamma_6\dot{\theta}^2 q_2 + \gamma_6\ddot{q}_2 + \gamma_4\ddot{\theta})\delta q_1 + (\gamma_6\ddot{q}_1 - \gamma_6\dot{\theta}^2 q_1 \\
&- \gamma_3\dot{\theta}^2 q_2 + \gamma_5\ddot{\theta} + \gamma_3\ddot{q}_2)\delta q_2]\mathrm{d}t
\end{aligned}
\tag{28}
$$

The elastic potential energy of the robotic hand's flexible arm is:

$$\delta \int_{t_1}^{t_2} E_{ul}\mathrm{d}t = \int_{t_1}^{t_2} EI[(\eta_1 q_1 + \eta_3 q_2)\delta q_1 + (\eta_2 q_1 + \eta_4 q_2)\delta q_2]\mathrm{d}t \tag{29}$$

The kinetic energy of the robotic hand is:

$$
\begin{aligned}
\delta \int_{t_1}^{t_2} E_{km}\mathrm{d}t = \int_{t_1}^{t_2} &-m[(\beta_2{}^2\dot{\theta}q_2{}^2 + 2\beta_1{}^2\dot{\theta}\dot{q}_1 q_1 + \beta_1 l\ddot{q}_1 + \beta_2 l\ddot{q}_2 + 2\beta_2{}^2\dot{\theta}\dot{q}_2 q_2 \\
&+ \beta_1{}^2\dot{\theta}q_1{}^2 + \dot{\theta}l^2 + 2\beta_1\beta_2\dot{\theta}\dot{q}_1 q_2 + 2\beta_1\beta_2\dot{\theta}\ddot{q}_2 q_1 + 2\beta_1\beta_2\dot{\theta}\dot{q}_1 q_2)\,\delta\theta \\
&+ (-\dot{\theta}^2 q_2\beta_2\beta_1 + \beta_1{}^2\ddot{q}_1 + \ddot{\theta}l\beta_1 + \beta_2\ddot{q}_2\beta_1 - \dot{\theta}^2 q_1\beta_1{}^2)\delta q_1 + (\ddot{\theta}l\beta_2 \\
&+ \beta_2{}^2\ddot{q}_2 + \beta_1\ddot{q}_1\beta_2 - \dot{\theta}^2 q_1\beta_1\beta_2 - \dot{\theta}^2 q_2\beta_2{}^2)\delta q_2]\mathrm{d}t
\end{aligned}
\tag{30}
$$

The virtual work performed by the system is:

$$\delta \int_{t_1}^{t_2} W\mathrm{d}t = \int_{t_1}^{t_2} \tau\delta\theta\mathrm{d}t \tag{31}$$

Substituting the above formulas into Hamilton's equations and setting the coefficients of the terms containing δq_1 and δq_2 to zero, the dynamic equation of the robotic hand was obtained as:

$$\begin{bmatrix} M_{11} & M_{12} \\ M_{21} & M_{22} \end{bmatrix} \begin{bmatrix} \ddot{q}_1 \\ \ddot{q}_2 \end{bmatrix} + \begin{bmatrix} K_{11} & K_{12} \\ K_{21} & K_{22} \end{bmatrix} \begin{bmatrix} q_1 \\ q_2 \end{bmatrix} + \begin{bmatrix} D_1 \\ D_2 \end{bmatrix} = 0 \qquad (32)$$

where, $M_{11} = -m\beta_1^2 - \rho A\gamma_2$, $M_{12} = -m\beta_2\beta_1 - \rho A\gamma_6$, $M_{21} = -m\beta_2\beta_1 - \rho A\gamma_6$, $M_{22} = -m\beta_2^2 - \rho A\gamma_3$, $K_{11} = \rho A\dot{\theta}^2\gamma_2 - EI\eta_1 + m\dot{\theta}^2\beta_1^2$, $K_{12} = m\dot{\theta}^2\beta_2\beta_1 + \rho A\dot{\theta}^2\gamma_6 - EI\eta_3$, $K_{21} = -EI\eta_2 + m\dot{\theta}^2\beta_2\beta_1 + \rho A\dot{\theta}^2\gamma_6$, $K_{22} = m\dot{\theta}^2\beta_2^2 - EI\eta_4 + \rho A\dot{\theta}^2\gamma_3$, $D_1 = -m\ddot{\theta}l\beta_1 - \rho A\ddot{\theta}\gamma_4$, $D_2 = m\ddot{\theta}l\beta_2 - \rho A\ddot{\theta}\gamma_5$, $\beta_1 = \Phi_1(l)$, $\beta_2 = \Phi_2(l)$, $\gamma_1 = \int_0^l x^2 dx$, $\gamma_2 = \int_0^l \Phi_1(x)^2 dx$, $\gamma_3 = \int_0^l \Phi_2(x)^2 dx$, $\gamma_4 = \int_0^l x\Phi_1(x)dx$, $\gamma_5 = \int_0^l x\Phi_2(x)dx$, $\gamma_6 = \int_0^l \Phi_1(x)\Phi_2(x)dx$, $\eta_1 = \int_0^l \left(\frac{d^4\Phi_1}{dx^4}\right)\Phi_1 dx$, $\eta_2 = \int_0^l \left(\frac{d^4\Phi_2}{dx^4}\right)\Phi_1 dx$, $\eta_3 = \int_0^l \left(\frac{d^4\Phi_1}{dx^4}\right)\Phi_2 dx$, $\eta_4 = \int_0^l \left(\frac{d^4\Phi_2}{dx^4}\right)\Phi_2 dx$.

Considering gravity, the elastic potential energy, E_{pl}, of the flexible arm and the gravitational potential energy, E_{pm}, of the end load were added to the system:

$$E_{pl} = \int_0^l \rho A g r_x(x, t) dx$$
$$E_{pm} = mg r_x(l, t) \qquad (33)$$

where r_x is the position vector component of r in the X_0 axis direction, and the system potential energy is provided by $V = E_{ul} + E_{pl} + E_{pm}$. Similarly, the dynamic equation of the robotic hand's flexible arm can be derived, with the modeling approach and methods primarily referring to the work of Liu et al. [43]. When establishing the kinematic model of the electric scalpel, selecting a truncation frequency of the first order is sufficient.

3.3. Workspace

The workspace of a robot is a crucial indicator for assessing its feasibility, as it reflects the robot's performance and directly impacts its practical application value [44]. An evaluation of the workspace of this robot system was conducted through experiments and simulations. As shown in Figure 13, the electric scalpel and the robotic arm were driven to their extreme positions three times, and the angles at each extreme position were measured, as shown in Table 2.
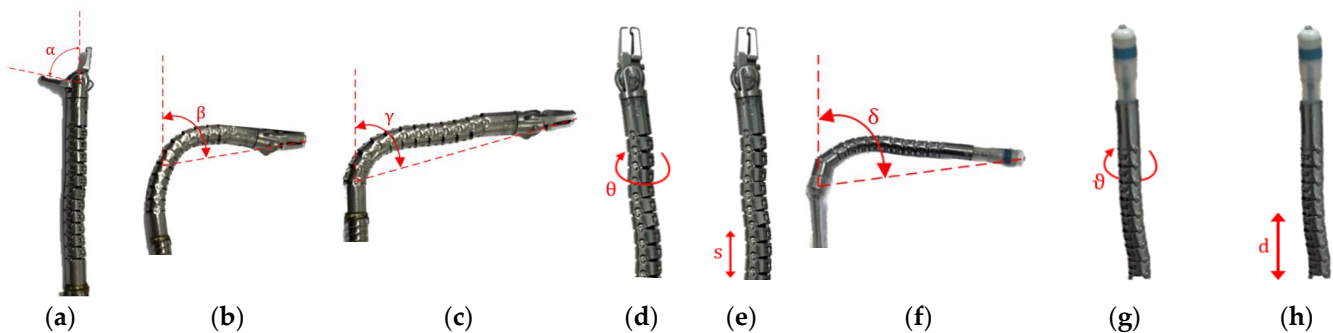

(a)   (b)   (c)   (d) (e)   (f)   (g)   (h)

Figure 13. Motion parameters of the robot system. (**a**) Motions 1 and 2: obtaining the gripper's opening angle. (**b**) Motion 3: obtaining the angle of movement of the distal flexible mechanical arm. (**c**) Motion 4: obtaining the angle of movement of the proximal flexible mechanical arm. (**d**) Motion 5: obtaining the overall rotation angle of the robot. (**e**) Motion 6: obtaining the axial displacement of the robot. (**f**) Motion 7 obtaining the lateral bending angle of the electric scalpel. (**g**) Motion 8: obtaining the rotation angle of the electric scalpel. (**h**) Motion 9: obtaining the axial displacement of the electric scalpel.

Table 2. The parameters of ankle movements.

	$\alpha/°$	$\beta/°$	$\gamma/°$	$\theta/°$	s/mm	$\delta/°$	$\vartheta/°$	d/mm
First Test	87	82	79	360	30	85	360	30
Second Test	85	84	84	360	30	83	360	30
Third Test	86	85	80	360	30	86	360	30
Average	86	83.6	81	360	30	84.6	360	30

The robot that has been designed theoretically should be capable of achieving movements in each direction of up to 90 degrees. However, the actual measurements indicate deviations ranging from 3 to 11 degrees less than the theoretical angles. These discrepancies can be attributed to factors such as insufficient machining precision and assembly errors, which introduce some errors during the motion. Using the Monte Carlo random sampling method, a large number of end-effector position points were plotted to visualize the robot's workspace. Here, 8000 sets of random points were generated within a finite range, and the results were displayed in a three-dimensional coordinate system, as shown in Figure 14. Finally, the effective workspace for s = 0 and d = 0 was obtained, where the red point set represents the experimental workspace of the limit position test, with the average value of the test taken as the constraint, and the blue point set represents the theoretical workspace, with theoretical angles taken as constraints.

(**a**)

(**b**)
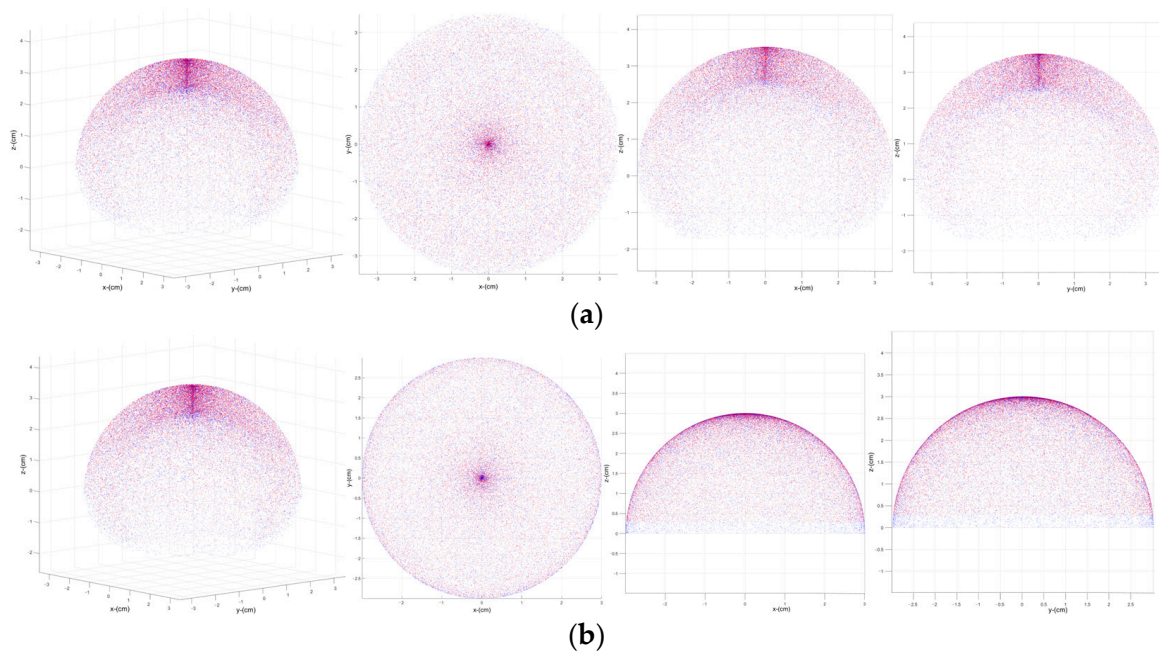
Figure 14. Robotic workspace. (**a**) Workspace and three views of the robotic arm. (**b**) Workspace and three views of the electric knife.

The visualization results of the workspace indicated that the robot can move in a circular motion along the front end of the endoscope, covering a wide range. The small difference between the test range and the theoretical range suggests that the robot system can reach the target surgical area effectively, providing a strong reference for practical applications.

4. Experimental Testing

4.1. Grasping Force Test

The gripping capability of the robotic arm was tested to verify the system's effective payload, with the experimental setup shown in Figure 15a. The experiment aimed to validate whether the robotic arm with the drive system could achieve a gripping force of 3 N, as this force suffices for most routine surgical procedures, such as knotting and

suturing [45]. Due to the small size of the robotic arm's grippers, direct measurement of their gripping force is challenging. Therefore, the experiment was designed to test the gripping force of one gripper. During the testing process, the zero-setting adjustment was applied to the spring force gauge. Initially, one end of the rope was fastened to a clamp in an open state, while the other end was horizontally connected to the spring force gauge, with the rope being taut, and the gauge fixed. Subsequently, the tested clamp was driven to perform a closing motion, thereby pulling the rope to generate a reading on the spring force gauge. Similarly, we assessed the retraction force of the robotic arm, where the clamp started in a closed position. By controlling the tested clamp to open, readings were obtained to complete the measurement, as depicted in Figure 15b. After multiple measurements, the results exceeded 3 N, indicating that the robotic arm's grip strength exceeded 3 N, rendering it suitable for routine surgical procedures.
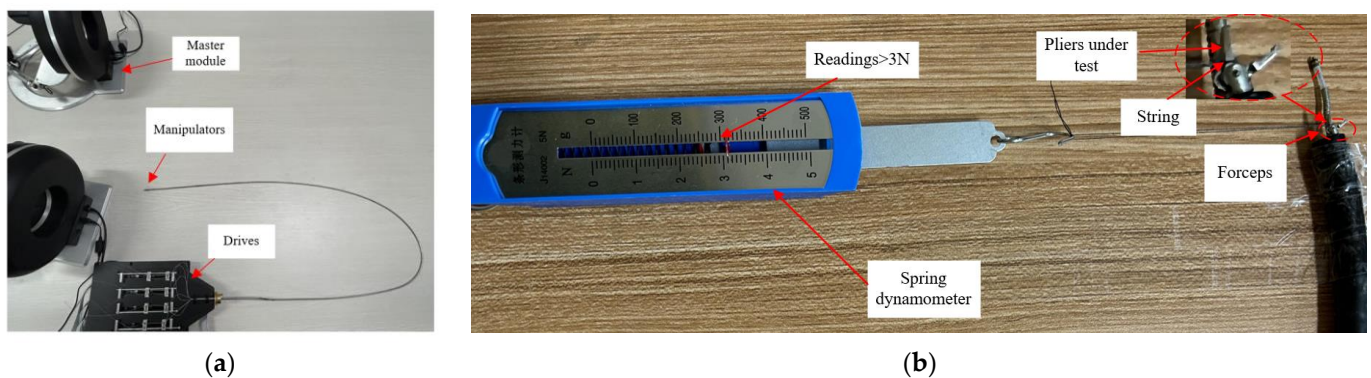

(**a**)

(**b**)

Figure 15. Grasping force testing platform. (**a**) Prototype of the robotic arm with the integrated drive system. (**b**) Experimental results.

4.2. Performance Testing

To validate the system's precision, experiments were conducted under primary manual control to harvest green and red peppers, as well as melon seeds, as illustrated in Figure 16. The robotic arm and electric knife performed the harvesting experiment through the endoscope platform, positioning the peppers and melon with seeds in front of the endoscope platform to represent the objects of operation. Initially, the operator used the primary control device to maneuver the robot to the target area of the pepper. Subsequently, the robotic arm was manipulated to extend and open the gripper. The position of the electric knife was then adjusted to complete the cutting action, while the gripper simultaneously picked the seeds. Finally, the robot's flexible arm retracted and released the seeds. Despite the small size of the target objects (diameter of the pepper seeds < 3 mm; length of the melon seeds < 6 mm, width < 2 mm), the robotic prototype was able to complete gripping, rotating, cutting, and releasing operations, as demonstrated in Table 3. Through these fundamental operations, the system's precision was tested, and the flexibility and coordination of the system under master–slave configuration were preliminarily validated.

Table 3. Test performance.

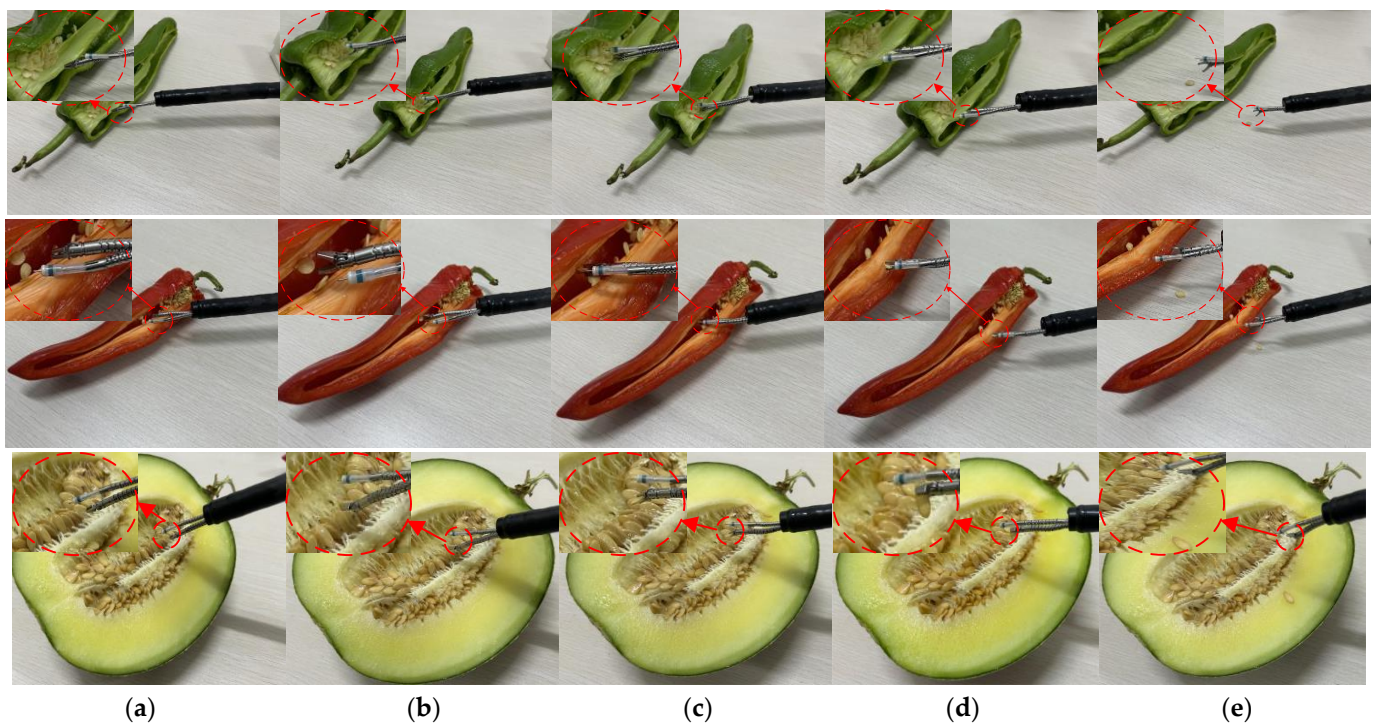| Surgical Object	Average Diameter (mm)	Minimum Diameter (mm)	Average Thickness (mm)	Surface	Duration (s)
Green pepper seeds	2.7	2.5	0.7	Rough and dry	45
Red pepper seeds	2.9	2.7	0.6	Rough and dry	47
Melon seeds	5.2	4.7	1.9	Smooth and moist	55

Figure 16. Performance testing. (**a**) Controlling the robotic arm to reach the target area. (**b**) Extending the flexible arm and gripping the target. (**c**) Adjusting the electric scalpel's position and completing the cutting. (**d**) Retracting the robot. (**e**) Discarding the seeds.

4.3. In Vitro Experiments

To further validate the effectiveness of the design, we conducted in vitro experiments. The experimental setup, as shown in Figure 17, included the robot, endoscope platform, pig stomach, and a monitor. In the actual operation, the robot needed to be controlled remotely through the respective channels of the endoscope. First, the endoscope was inserted into the pig stomach. Once the endoscope reached the appropriate position, the robotic arm and electric scalpel were inserted into the respective channels of the endoscope. The endoscope was connected to the monitor via cables, and the pig stomach was inflated before the procedure.

First, we demonstrated the scenario after the endoscope platform reached the appropriate area of the stomach wall. Once the endoscope was secured, the robotic arm and electric scalpel were inserted into the endoscope system. When the robot reached the target area, a series of tests were performed inside the pig's stomach, including robot translation, bending, rotation, gripper manipulation, and electric scalpel cutting, as shown in Figure 18. The robot successfully completed translation and rotation tests, demonstrating minimal friction between the robot's drive components and the endoscope platform channels. The bending and rotation experiments confirmed the robot's flexibility, with the robot demonstrating sufficient torque to perform various movements. Finally, the gripper was able to open and close successfully in the confined space, and the electric scalpel completed the cutting task.

All the experimental results indicated that the designed robot exhibits a high degree of flexibility and practicality both in vitro and in vivo. This provides a solid foundation for future more in-depth in vivo experiments. The actual human stomach environment is exceptionally complex, with factors such as narrow spaces and soft tissue interference, which can impact the robot's flexibility and grasping capabilities. Therefore, these tests were conducted to verify the robot's flexibility and grasping capabilities in real-world operations. At the same time, these experiments simulated real operational processes and validated the accuracy of the control system and operating procedures.
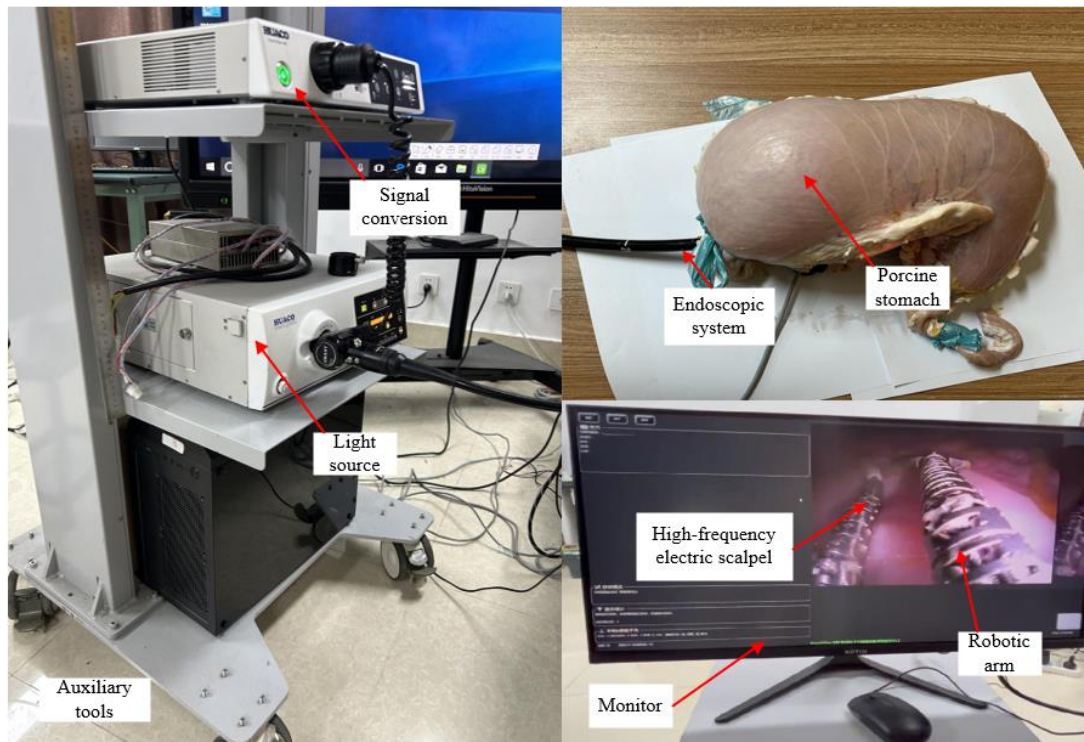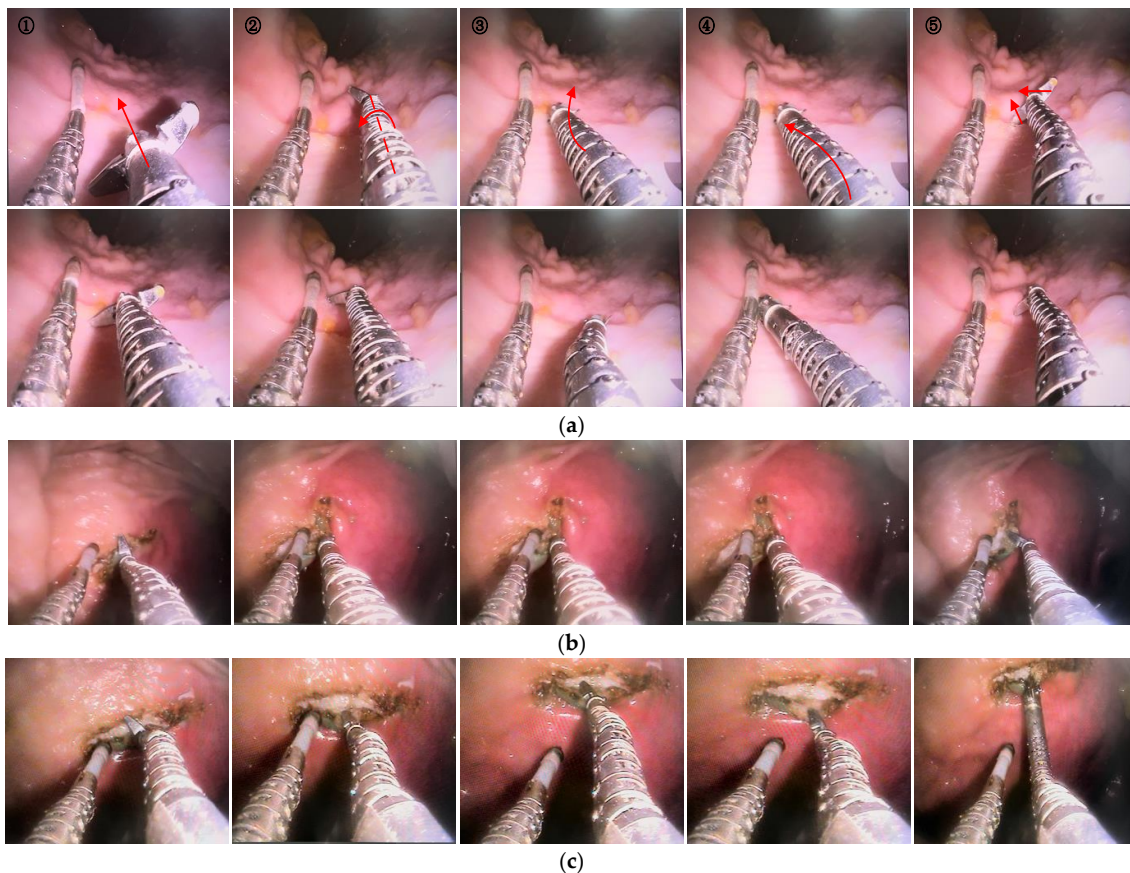
Figure 17. In vitro experiment platform.

Figure 18. Experimental process. (**a**) Robotic arm movements. ① Translation, ② rotation, ③ bending of the distal arm, ④ bending of the proximal arm, and ⑤ gripper closure. (**b**) Electric scalpel cutting. (**c**) Robotic arm gripping the target.

5. Conclusions and Future Work

This study proposed a flexible continuum robotic system for minimally invasive gastrointestinal endoscopic surgery. The system reduced the size of both the driver and the actuator while maintaining high flexibility to alleviate postoperative discomfort for patients. The robot's flexible robotic arms were designed with a hollow structure and integrated with wire ropes with hoses for driving. The diameter of the robotic arm is 3.4 mm, while the electric knife's diameter is 2.8 mm, with a total of nine degrees of freedom.

This article provided a detailed description of the robotic system, including the manipulator system and the drive system. The theoretical analysis of robotics provides the foundation for motion control. The robot's workspace was evaluated through experiments and simulations, including the opening and closing angles of the robotic arm grippers, bending angles of the robot's far and near flexible robotic arms, and the translation distance of the robot. Relevant experiments validated the robot's ideal gripping force and flexibility, demonstrating that the robot's effective payload exceeds 3 N, meeting the requirements of most routine operations. By using the primary manipulator to control the robot to grasp green and red peppers and melon seeds, the system's precision was showcased, preliminarily validating the performance of the robotic arm's flexibility and operational coordination. In vitro experiments were conducted to demonstrate the operation process of surgical procedures, showcasing the rationality and efficiency of the workflow.

However, this study also has some limitations. The robot system was designed with only a robotic arm with flexible arms and a high-frequency electric knife, while a complete minimally invasive gastrointestinal endoscopic surgery requires multiple tools. Therefore, further development of additional manipulators will be pursued to achieve collaborative operation. Additionally, force feedback sensors can be utilized to enhance the functionality of the flexible arm grippers, and closed-loop precise control can be achieved by integrating deep learning and monocular depth estimation techniques to determine the robot's pose [46]. Finally, more in vitro experiments will be conducted to verify the safety and effectiveness of the robot system, thus realizing the practical application of the system.

Author Contributions: Conceptualization, L.S.; methodology, L.S. and X.C.; software, L.S.; validation, L.S.; formal analysis, L.S.; writing—original draft preparation, L.S.; writing—review and editing, L.S. and X.C.; visualization, L.S.; resources, L.S.; supervision, X.C.; project administration, X.C.; funding acquisition, L.S. All authors have read and agreed to the published version of the manuscript.

Data Availability Statement: The original data contributions presented in this study are included in the article. Further inquiries can be directed to the corresponding authors.

Conflicts of Interest: The authors declare no conflicts of interest.

References

1. Ferlay, J.; Colombet, M.; Soerjomataram, I.; Parkin, D.M.; Piñeros, M.; Znaor, A.; Bray, F. Cancer statistics for the year 2020: An overview. *Int. J. Cancer* **2021**, *149*, 778–789. [CrossRef] [PubMed]
2. Omisore, O.M.; Han, S.; Xiong, J. A Review on Flexible Robotic Systems for Minimally Invasive Surgery along with some of the technical and technological challenges hindering their prominence. *IEEE Trans. Syst. Man Cybern. Syst.* **2020**, *52*, 631–644. [CrossRef]
3. Burgner-Kahrs, J.; Rucker, D.C.; Choset, H. Continuum robots for medical applications: A survey. *IEEE Trans. Robot.* **2015**, *31*, 1261–1280. [CrossRef]
4. Yung, K.; Cheung, J.; Chung, S.; Singh, S.; Yeung, C. A single-port robotic platform for laparoscopic surgery with a large central channel for additional instrument. *Ann. Biomed. Eng.* **2017**, *45*, 2211–2221. [CrossRef] [PubMed]
5. Piccigallo, M.; Scarfogliero, U.; Quaglia, C.; Petroni, G.; Valdastri, P. Design of a novel bimanual robotic system for single-port laparoscopy. *IEEE/ASME Trans. Mechatron.* **2010**, *15*, 871–878. [CrossRef]
6. Kim, C.G. Natural orifice transluminal endoscopic surgery and upper gastrointestinal tract. *J. Gastric Cancer* **2013**, *13*, 199–206. [CrossRef] [PubMed]
7. Li, Y.; Richter, F.; Lu, J.; Funk, E.K.; Orosco, R.K.; Zhu, J.; Yip, M.C. Super: A surgical perception framework for endoscopic tissue manipulation with surgical robotics. *IEEE Robot. Autom. Lett.* **2020**, *5*, 2294–2301. [CrossRef]

8. Choi, H.; Kwak, H.; Lim, Y.; Kim, H. Surgical robot for single-incision laparoscopic surgery. *IEEE Trans. Bio-Med. Eng.* **2014**, *61*, 2458. [CrossRef] [PubMed]

9. Poon, H.; Li, C.; Gao, W.; Ren, H.; Lim, C.M. Evolution of robotic systems for transoral head and neck surgery. *Oral Oncol.* **2018**, *87*, 82–88. [CrossRef]

10. Zhao, J.; Feng, B.; Zheng, M.H.; Xu, K. Surgical robots for SPL and NOTES: A review. *Minim. Invasive Ther.* **2015**, *24*, 8–17. [CrossRef]

11. Quaglia, C.; Petroni, G.; Niccolini, M.; Caccavaro, S.; Dario, P. Design of a compact robotic manipulator for single-port laparoscopy. *J. Mech. Des.* **2014**, *136*, 105001. [CrossRef]

12. Ren, H. Computer-assisted transoral surgery with flexible robotics and navigation technologies: A review of recent progress and research challenges. *Crit. Rev. Biomed. Eng.* **2013**, *41*, 4–5. [CrossRef] [PubMed]

13. Zhan, Y.; Duan, X.G.; Cui, T.F.; Han, D.Q. Craniotomy robot system based on human-machine parallel collaboration. In Proceedings of the 2016 IEEE International Conference on Mechatronics and Automation, Heilongjiang, China, 7–10 August 2016; pp. 1119–1124.

14. Li, C.; Gu, X.; Xiao, X.; Lim, C.M.; Ren, H. A robotic system with multichannel flexible parallel manipulators for single port access surgery. *IEEE Trans. Ind. Inform.* **2019**, *15*, 1678–1687. [CrossRef]

15. Hu, Y.; Zhang, L.; Li, W.; Yang, G.-Z. Design and fabrication of a 3-d printed metallic flexible joint for snake-like surgical robot. *IEEE Robot. Autom. Lett.* **2019**, *4*, 1557–1563. [CrossRef]

16. Sun, Y.; Song, S.; Liang, X.; Ren, H. A miniature soft robotic manipulator based on novel fabrication methods. *IEEE Robot. Autom. Lett.* **2016**, *1*, 617–623. [CrossRef]

17. Jin, X.; Feng, M.; Zhao, J.; Li, J. Design a flexible surgical instrument for robot-assisted minimally invasive surgery. In Proceedings of the 2016 IEEE International Conference on Robotics and Biomimetics (ROBIO), Qingdao, China, 3–7 December 2016; pp. 260–264.

18. Harvey, L.; Hendrick, R.; Dillon, N.; Blum, E.; Branscombe, L.; Webster, S.; Webster, R.J.; Anderson, T. A novel robotic endoscopic device used for operative hysteroscopy. *J. Minim. Invasive Gynecol.* **2020**, *27*, 1631–1635. [CrossRef] [PubMed]

19. Gao, H.; Zhang, Z.; Li, C.; Xiao, X.; Qiu, L.; Yang, X.; Hao, R.; Zuo, X.; Li, Y.; Ren, H. GESRsim: Gastrointestinal Endoscopic Surgical Robot Simulator. In Proceedings of the 2022 IEEE/RSJ International Conference on Intelligent Robots and Systems (IROS), Kyoto, Japan, 23–27 October 2022; pp. 9542–9549.

20. Ruszkowski, A.; Schneider, C.; Mohareri, O.; Salcudean, S. Bimanual teleoperation with heart motion compensation on the da Vinci Research Kit: Implementation and preliminary experiments. In Proceedings of the 2016 IEEE International Conference on Robotics and Automation (ICRA), Stockholm, Sweden, 16–21 May 2016; pp. 4101–4108.

21. Prasad, S.K.; Kitakawa, M.; Fischer, G.S. A modular 2-DOF force-sensing instrument for laparoscopic surgery. In Proceedings of the International Conference on Medical Image Computing and Computer Assisted Intervention, Montreal, QC, Canada, 15–18 November 2003; pp. 279–286.

22. Tavakoli, M.; Patel, R.V.; Moallern, M. Haptic interaction in robot-assisted endoscopic surgery: A sensorized end-effector. *Int. J. Med. Robot. Comput. Assist. Surg.* **2005**, *1*, 53–63. [CrossRef] [PubMed]

23. Thielmann, S.; Seibold, U.; Haslinger, R.; Passing, G. MICA-a new generation of versatile instruments in robotic surgery. In Proceedings of the 2010 IEEE/RSJ International Conference on Intelligent Robots and Systems, Taipei, Taiwan, 18–22 October 2010; pp. 871–878.

24. Lau, K.; Leung, E.; Chiu, W.; Yam, Y.; Lau, J.; Poon, C. A flexible surgical robotic system for removal of early-stage gastrointestinal cancers by endoscopic submucosal dissection. *IEEE Trans. Ind. Inform.* **2016**, *12*, 2365–2374. [CrossRef]

25. Feng, M.; Fu, Y.; Pan, B.; Liu, C. Development of a medical robot system for minimally invasive surgery. *Int. J. Med. Robot. Comput. Assist. Surg.* **2012**, *8*, 85–96. [CrossRef]

26. Tay, G.; Tan, H.; Nguyen, T.K.; Phee, S.J.; Iyer, N.G. Use of the EndoMaster robot-assisted surgical system in transoral robotic surgery: A cadaveric study. *Int. J. Med. Robot. Comput. Assist. Surg.* **2018**, *14*, e1930. [CrossRef]

27. Zorn, L.; Nageotte, F.; Zanne, P.; Legner, A.; Dallemagne, B. A Novel Telemanipulated Robotic Assistant for Surgical Endoscopy: Preclinical Application to ESD. *IEEE Trans. Biomed. Eng.* **2018**, *65*, 797–808. [CrossRef] [PubMed]

28. Li, C.; Gu, X.; Xiao, X.; Lim, C.M.; Ren, H. Flexible robot with variable stiffness in transoral surgery. *IEEE/ASME Trans. Mechatron.* **2020**, *25*, 1–10. [CrossRef]

29. de Moura, D.T.H.; Aihara, H.; Jirapinyo, P.; Farias, G.; Hathorn, K.E.; Bazarbashi, A.; Thompson, C.C. Robot-assisted endoscopic submucosal dissection versus conventional ESD for colorectal lesions: Outcomes of a randomized pilot study in endoscopists without prior ESD experience (with video). *Gastrointest. Endosc.* **2019**, *90*, 290–298. [CrossRef]

30. Chiu, P.; Ho, K.Y.; Jay, S. Colonic endoscopic submucosal dissection using a novel robotic system (with video). *Gastrointest. Endosc.* **2020**, *93*, 1172–1177. [CrossRef] [PubMed]

31. Wu, L.; Song, S.; Wu, K. Development of a compact continuum tubular robotic system for nasopharyngeal biopsy. *Med. Biol. Eng. Comput.* **2017**, *55*, 403–417. [CrossRef] [PubMed]

32. Hong, W.Z.; Xie, L.; Liu, J.; Sun, Y.; Li, K.; Wang, H. Development of a Novel Continuum Robotic System for Maxillary Sinus Surgery. *IEEE/ASME Trans. Mechatron.* **2018**, *23*, 1226–1237. [CrossRef]

33. Morimoto, T.K.; Hawkes, E.W.; Okamura, A.M. Design of a Compact Actuation and Control System for Flexible Medical Robots. *IEEE Robot. Autom. Lett.* **2017**, *2*, 1579–1585. [CrossRef] [PubMed]

34.   Meng, Q.; Liu, G.; Xu, X.; Meng, Q.; Qin, L.; Yu, H. Design and Analysis of a Supine Ankle Rehabilitation Robot for Early Stroke Recovery. *Machines* **2023**, *11*, 787. [CrossRef]

35.   Barrientos-Diez, J.; Dong, X.; Axinte, D.; Kell, J. Real-Time Kinematics of Continuum Robots: Modeling and Validation. *Robot. Comput.-Integr. Manuf.* **2021**, *67*, 102019. [CrossRef]

36.   Tan, C.; Xu, P.; Li, P.; Yu, H. Current Research on Modeling and Control Methods for Cable-driven Flexible Manipulator. *Inf. Control* **2023**, *52*, 277–291.

37.   Dwivedy, S.K.; Eberhard, P. Dynamic Analysis of Flexible Manipulators: A Literature Review. *Mech. Mach. Theory* **2006**, *41*, 749–777. [CrossRef]

38.   Chen, W.; You, X.; Cui, X.; Yu, S. Dynamics Modeling and Tension Analysis for a Cable-Driven Humanoid-Arm Robot. *J. Beijing Univ. Aeronaut. Astronaut.* **2013**, *39*, 335–339.

39.   Yang, Z. *Mechanical Vibration and Noise*; Higher Education Press: Beijing, China, 2011.

40.   Guo, Z.; Jin, G.; Chang, B.; Wang, Y. Research of Dynamic Modeling and Performance for Rigid-Flexible Manipulators. *J. Tianjin Polytech. Univ.* **2013**, *32*, 70–74.

41.   Heidari, H.R.; Korayem, M.H.; Haghpanahi, M.; Batlle, V.F. A New Nonlinear Finite Element Model for the Dynamic Modeling of Flexible Link Manipulators Undergoing Large Deflections. In Proceedings of the 2011 IEEE International Conference on Mechatronics, Istanbul, Turkey, 13–15 April 2011; pp. 375–380.

42.   Meng, S.; Xiong, J.; Lv, Z. Modeling of Arm System of Folding-Boom Aerial Platform Vehicle. *Noise Vib. Control* **2012**, *32*, 63–67.

43.   Liu, X.; Huang, Y.; Cui, P.; Xu, Z. Modeling and Dynamic Characteristic Analysis of Flexible Robotic Arm. *Noise Vib. Control* **2014**, *34*, 7.

44.   Meng, Q.; Liu, G.; Meng, Q.; Xu, X.; Qin, L.; Yu, H. Bionic Design of a Novel Portable Hand-Elbow Coordinate Exoskeleton for Activities of Daily Living. *Electronics* **2023**, *12*, 3326. [CrossRef]

45.   Okamura, A.M. Methods for haptic feedback in teleoperated robot-assisted surgery. *Ind. Robot-Int. J.* **2004**, *31*, 499–508. [CrossRef]

46.   Kuo, Y.-L.; Liu, B.-H.; Wu, C.-Y. Pose Determination of a Robot Manipulator Based on Monocular Vision. *IEEE Access* **2016**, *4*, 8454–8464. [CrossRef]